# Nanostabilization of tetragonal distorted FeCo variants in ultra-thin FeCo/TiN multilayer films

Niklas Wolff [a], Philipp Jordt [b], Justin Jetter [c], Henning Vogt [b], Andriy Lotnyk [d], Klaus Seemann [e], Sven Ulrich [e], Eckhard Quandt [c], Bridget M. Murphy [b], Lorenz Kienle [a,*]

[a] *Synthesis and Real Structure, Institute for Materials Science, Kiel University, 24143 Kiel, Germany*
[b] *Institute for Experimental and Applied Physics, Kiel University, 24118 Kiel, Germany*
[c] *Inorganic Functional Materials, Institute for Materials Science, Kiel University, 24143 Kiel, Germany*
[d] *Leibniz Institute of Surface Engineering (IOM), 04318 Leipzig, Germany*
[e] *Institute for Applied Materials (IAM-AWP), Karlsruhe Institute of Technology (KIT), 76344 Eggenstein-Leopoldshafen, Germany*

## ABSTRACT

Composites of ultra-thin nanolayers of FeCo/TiN with individual layer thickness of a few unit cells offer stability at elevated temperatures and exhibit defined magnetic properties which can be tuned by varying the layers thickness making them interesting candiates as components for magnetoelectric (ME) sensors. Initial studies describing the nanostructure of such thin films, however, left uncertainty about their exact crystal structure. With aberration-corrected microscopes the characterization of the local structure down to the atomic scale is possible to address the real structure with high precision. Here, by means of atomic resolution TEM imaging together with X-ray diffraction analysis, we were able to describe the nanostructure to be composed of individual layers of FeCo and TiN forming a superlattice with a defined cube-on-cube orientation relationship. The simulation of electron diffraction pattern featuring superlattice reflections on basis of structural modeling together with geometric phase analysis verified a defined orientation relationship resolving in the nanostabilization of a tetragonal distorted FeCo unit cell with c/a < 1.

## 1. Introduction

Multilayer architectures of FeCo and TiN have been designed and examined in the past by Klever *et al.* [1]. For the purpose of smart wear protection coatings with self monitoring functions. The combination of high hardness and temperature resistivity of TiN and the tunable magnetic characteristics of the ferromagnetic alloy FeCo suggests multilayers of FeCo/TiN for the magnetic phase in magnetoelectric (ME) composite sensors, e.g., for biomagnetic imaging [2,3]. In this respect, the magnetic properties of the composite can be effectively tuned by the layer thickness of FeCo and TiN layers, demonstrating a low coercive field of $\mu_0 H_c$ 0.30 mT and a saturation magnetization of $\mu_0 H_s$ 0.4 T usingFeCo layers of about 1 nm in thickness [1]. In general, the reduction of the FeCo layer thickness down to the nanoscale is known to gradually "soften" the magnetic characteristics yielding a low coercive field at high saturation magnetization [4–6]. In ME composites, the available biomagnetic signal is in principal read out by a voltage change which is induced via the transfer of magnetostrictive strain arising in a soft magnetic material such as FeCoSiB onto a piezoelectric material such as AlN [7–9]. In the ME magnetic field sensor these FeCoSiB/AlN composites are deposited onto silicon substrates and shaped into cantilever geometry. One promising approach is to detect magnetic fields by using the magnetoelastic properties of the magnetostrictive part via the $\Delta E$-effect, which is the effective softening of the Youngs modulus $E$ of a magnetostrictive material in the small strain regime [10,11]. Herein, the easy measurable frequency shift of the resonance frequency upon application of an alternating external magnetic bias field results in the elastic softening of the magnetic phase and proved high sensitivity in the order of 100 pT/Hz$^{-1}$ at the biomagnetic relevant low frequency regime between 10 and 100 Hz [12]. The limit of detection of these sensors was theoretically calculated and demonstrated to show improvement by an increase in the quality factor $Q$, e.g. by device geometry or by operation

---

in vacuum. The $\Delta E$-based ME sensors benefit significantly more on an improvement of $Q$ than conventional ME sensors when magnetic noise can be suppressed efficiently [13]. However, the MEMS process flow for vacuum encapsulation includes elevated temperatures which exceed the temperature stability of the magnetic properties of the amorphous FeCoSiB [14]. In this respect, nanolayers of crystalline FeCo/TiN potentially offer defined magnetic properties together with temperature stability up to 600 °C.

The thin film architecture and the nanostructure of the individual components are important parameters for the magnetostriction behavior in those systems. Fukzawa et al. [15] demonstrated that the saturation magnetostriction can be largely influenced by the interface quality and resulting internal stress in FeCo. The structure analysis is therefore decisive to control the micro- and nanostructure of the layered architecture with respect to deposition parameters to achieve a potentially high quality magnetic phase with large magnetostriction as component for ME sensors. Reports on the multilayer architecture including nanostructure analysis have been initially published by Klever et al. [16] using Auger electron spectroscopy, X-ray diffraction (XRD) and electron diffraction (ED) techniques as well as high-resolution transmission electron microscopy (HRTEM) imaging. The studied FeCo/TiN architectures demonstrated temperature stability up to 600 °C and a strongly textured and columnar growth was observed. Refering to Klever et al., the nanostructural details were subject of two major hypothesis: (i) The multilayer thin film architecture as well as the growth conditions result in the incorporation of a high volume fraction of Fe and Co atoms into an fcc TiN lattice by sequential magnetron sputter deposition, (ii) a (Ti,Fe, Co)N solid solution in a pseudo-fcc crystal structure is formed as a consequence of collision induced atomic mixing and subsequent nanostabilization.

For this work, we used atomic resolution microscopy and report about nanostructure investigation and structural modeling on a similar FeCo/TiN multilayer in order to address the hypothesis. The results imply the formation of a textured superlattice composed of individual layers of FeCo (CsCl-structure) and TiN (NaCl-structure) showing a defined cube-on-cube orientation relation. As a result of the in-plane lattice mismatch, tensile in-plane strain was observed for the FeCo unit cell resulting in the nanostabilization of tetragonal distorted variants.

## 2. Materials and methods

The investigated multilayer film of [FeCo(0.7 nm)/TiN(1.6 nm)]$_{153}$ with a nominal thickness of 400 nm was deposited during former work reported by Klever et al. [1] by non-reactive magnetron sputter deposition on a modified Leybold Z550 sputter setup using targets of FeCo and TiN with 99.9% chemical purity and 150 mm in diameter. For sputtering of multilayers, SiO$_2$/Si substrates were placed onto a rotatable substrate table at a distance of 50 mm to the target surfaces. The target surfaces were sputter cleaned for 15 min. in a pure Ar atmosphere (6.0 purity) at 0.5 Pa total pressure prior to deposition at a base pressure of $< 1 \times 10^{-6}$ mbar in the vacuum chamber. Preconditioning of the substrate surfaces took place under the same conditions for 20 min at a substrate bias voltage of 320 V sustained by an RF plasma. The Ar total pressure during the film deposition process was 0.2 Pa in order to sustain a DC plasma in front of the TiN target by supplying 700 W DC power while maintaining a RF plasma (250 W power) in front of the FeCo target. After determining the depositon rate, the multilayer was deposited by rotating the substrate in between the center positions of both targets.. An annealing step was performed after deposition for 60 min. in vacuum ($p < 1 \times 10{-}8$ mbar) at 600 °C in a static magnetic field of $\mu_0 H$ 50 mT.

The structure analysis on one individual as-deposited multilayer and one individual heated multilayer is performed using methods of transmission electron microscopy (TEM) and X-ray diffraction (XRD). The multilayers are deposited in the same process run, so it is assumed that they were structurally similar in the as-deposited state. In this respect, HRTEM enables the study of the atomic structure whereas the selected area electron diffraction (SAED) and energy-dispersive X-ray spectroscopy (EDS) in scanning mode give microstructural and spatially resolved chemical information of the multilayers, respectively. Large scale average information about the microstructure is obtained by Bragg X-ray diffraction, providing details about the crystallinity and strain on a macroscopic scale.

In addition, X-ray reflectivity (XRR) can assess the atomic and molecular scale interface structure even in the absence of a long-range order by providing access to the electron density across the entire multilayer. Thus we obtained average and localized data on the multilayer structure, the layer sequence and surface composition.

HRTEM and SAED data are collected on a Titan 80–300 microscope with an image-side spherical aberration (C$_S$)-corrector and subnanometer resolution. HRTEM micrographs are recorded under negative C$_S$ imaging (NCSI) [17] conditions exploiting the benefits of having a favorable contrast transfer function to allow for a direct interpretation of the projected crystal structure without the need to correlate the HRTEM micrographs with image simulations [18]. Such imaging conditions reduce the delocalization of object information to below the information limit of the microscope and generate an image displaying atomic columns as bright dots on a dark background. Scanning (S)TEM measurements including EDS are performed on a FEI Titan[3] G$^2$ 60–300 kV microscope operating at 300 keV. The TEM specimen preparation is performed by a focused ion beam (FIB) routine on a FEI Helios 600 dual beam FIB-SEM machine equipped with an Omniprobe micromanipulator following a standard lift-out procedure and subsequent ion-beam milling at 30 kV, 0.46 nA and 5 kV, 81 pA in the final stages to reduce possible ion-beam damage to the sample surface. Kinematic simulation of electron diffraction patterns and high-resolution phase contrast images are computed to verify the experimental data and NCSI imaging conditions using the JEMS program [19]. Processing of HRTEM micrographs included noise filtering [20] and is carried out via the Gatan Digital Micrograph 2.3 software package (DM).

The XRD experiments are performed on a Rigaku Micromax rotating anode radiating at the characteristic Cu-Kα energy with a wavelength of 1.54 Å. The beam size was $1 \times 1$ mm$^2$ (horizontal and vertical) with a resolution of $2 \times 10^{-4}$ Å$^{-1}$. The measurements are performed on a standard four circle diffractometer setup using the SPEC diffractometer software. Compution of experimental data sets is carried out using MATLAB and xrayutilities (build 1.5) program packages.

Pole-figure measurements are performed on a Rigaku SmartLab 9 kW XRD utilizing a rotation anode radiating at the characteristic Cu-Kα energy with a wavelength of 1.54 Å. The beam is scattered using a parabolic mirror to create a parallel X-ray beam at a tube voltage of 45 kV and a tube current of 200 mA. Construction and evaluation of the pole-figures is performed with the program Rigaku 3D Explore Version 3.1.1.0.

## 3. Results and discussion

### 3.1. Microstructure of FeCo/TiN thin films

The average microstructure of one as-deposited and one annealed FeCo/TiN multilayer is characterized by the combination of XRR measurements, Bragg XRD scans and SAED. The details of the nanostructure inherent to the FeCo/TiN mulitlayer are analyzed by structure models derived from electron and X-ray diffraction data along with HRTEM as discussed in the following. The temperature induced changes to the microstructure caused during the annealing procedure are discussed.

The XRR data collected on both, the as-deposited and the annealed multilayer are presented in Fig. 1a. The XRR is plotted up to wave vector of 0.7 Å$^{-1}$ to concentrate on the layer thickness. The electron density (Fig. 1b) is calculated from a model consisting of a sum of error functions modeling the layer structure. The fit was realized with the Parrat
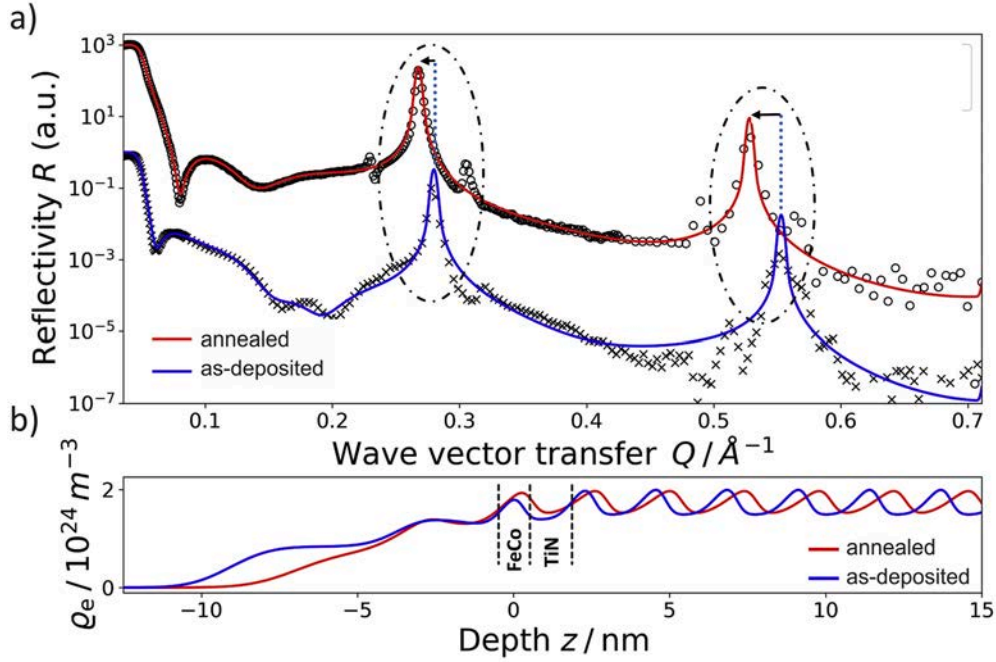
**Fig. 1.** (a) X-ray reflectivity curves of the as-deposited and annealed FeCo/TiN multilayers. The data indicates superlattice reflections at ~0.27 Å⁻¹ and ~ 0.52 Å⁻¹ moving towards smaller values as a consequence of annealing. (b) Calculated electron density variation denoted to the TiN capping layer and oscillations of the periodic superlattice. The depth value of 0 indicates the second FeCo layer counted from the surface.

algorithm [21] as model function and was refined using the Levenberg-Marquardt algorithm. The Fourier transform of the electron density was compared with the measured intensity and the electron density model recursively to obtain a good fit.

The reflectivity curves feature characteristic superlattice reflections, which represent the first and second order reflections of constructive interference of a multilayer on a solid substrate. The positions of these reflections are characteristic for $\Lambda$, the thickness of a single FeCo/TiN bilayer from the superlattice. After heating, the superlattice reflections show a position shift to smaller wave vectors, indicating a non-reversible lattice expansion relative to the as-deposited multilayer. From fitting the reflectivity data, the calculations showed an increase of the superlattice periodicity s from $\Lambda$ 22.826 ± 0.003 Å ($d_{FeCo}$ 6.8 ± 0.7 Å and $d_{TiN}$ 16.0 ± 0.7 Å) for the as-deposited multilayer up to $\Lambda$ 23.915 ± 0.003 Å ($d_{FeCo}$ 8.3 ± 0.4 Å and $d_{TiN}$ 15.6 ± 0.4 Å) for the annealed multilayer. According to the fit results the vertical thickness $d_{FeCo}$ of the FeCo layers in the superlattice increases by a remarkable value of 22%. The larger total $\Lambda$ implies an expansion of ~4.8% in film growth direction and may be explained by temperature induced lattice deformations such as the release of tensile lattice strains or unforeseen structural rearrangements. However, the measured periodicity length is in good agreement with the numbers reported by Klever ($\Lambda$ 2.6 nm). This impact of annealing is further supported by SAED analysis, given in Fig. A1, showing a position shift of the superlattice reflections in agreement with an increase in $\Lambda$. The calculated thickness of the individual components matches on average to six monolayers of FeCo ($d_{FeCo}$ 6.8 ± 0.7 Å) and seven monolayers of TiN ($d_{TiN}$ 16.0 ± 0.7 Å). The additional oscillations besides the superlattice reflections visible e.g. at 0.31 Å⁻¹ in the annealed multilayer, correspond to a typical length of 74 ± 5 Å and 79 ± 5 Å for the as-deposited and annealed multilayer, respectively. This modulation can be attributed to the combined thickness of the TiN capping layer and the first FeCo and TiN layers at the surface, which show signs of detoriation after annealing, as incidated by a lower electron density calculated and presented in Fig. 1b.

In more detail, the electron density which is derived from XRR (Fig. 1b) shows a continuous increase in the first 10 nm from the film surface before transforming into oscillations of the same amplitude.

With respect to the as-deposited multilayer, the oscillation period of the electron density is observed to increase for the annealed multilayer in consequence of the observed superlattice expansion. The electron density distribution at the surface accounts for a thick TiN capping layer deposited onto the last bilayer unit. The slow increasing electron density profile indicates high surface roughness of the capping layer, characterized by an amplitude of 10.3 ± 0.7 Å and 12.2 ± 0.4 Å for the as-deposited and annealed multilayer, respectively. The overall TiN capping layer thickness was measured giving 57.0 ± 1.7 Å and 36.0 ± 1.0 Å for the annealed multilayer sample. The smaller observed thickness, accompanied by lower atomic density and the increased surface roughness is attributed to deterioration of the protective capping layer by annealing.

Using X-ray Bragg diffraction, the crystal structure of the TiN layers was investigated by measuring the reciprocal space at the position of the TiN (002) reflection for the as-deposited and heated multilayer. In the following discussion we will always refer to the (002) TiN reflection as the majority component of the multilayer when addressing the out-of-plane reflections of the superlattice, if not otherwise identified. This diffraction data and the according fits are provided in Fig. 2. The displayed modulation of the intensity distribution around the measured Bragg position are described as Laue oscillations of 0.45 Å⁻¹ corresponding to a measure of 13 Å, which is in the same order of the TiN layer thickness in the superlattice as discussed in the XRR section above. [16,22] The fits are calculated by a least-square refinement of sum of three Gaussian functions to the data. To determine the original (002) Bragg reflection wave vector position, the mean position of the three reflections was determined to be 2.9646 ± 0.0013 Å⁻¹ for the as-deposited and 2.9649 ± 0.0013 Å⁻¹ for the annealed multilayer. This correlates to a lattice constant of $d_{(002)}$ 2.12 Å, which is in excellent agreement with the calculated position of the TiN (002) reflection and indicates TiN in its NaCl-type crystal structure. Further, the positions of the associated superlattice reflections around the TiN (002) reflection position are subjected to shifts in wave vector and intensity. That might hint to temperature related changes of the superlattice structure reflecting in the modulation of c-axis intensities. However, there was no definite observation of chemical intermixing on annealed specimens
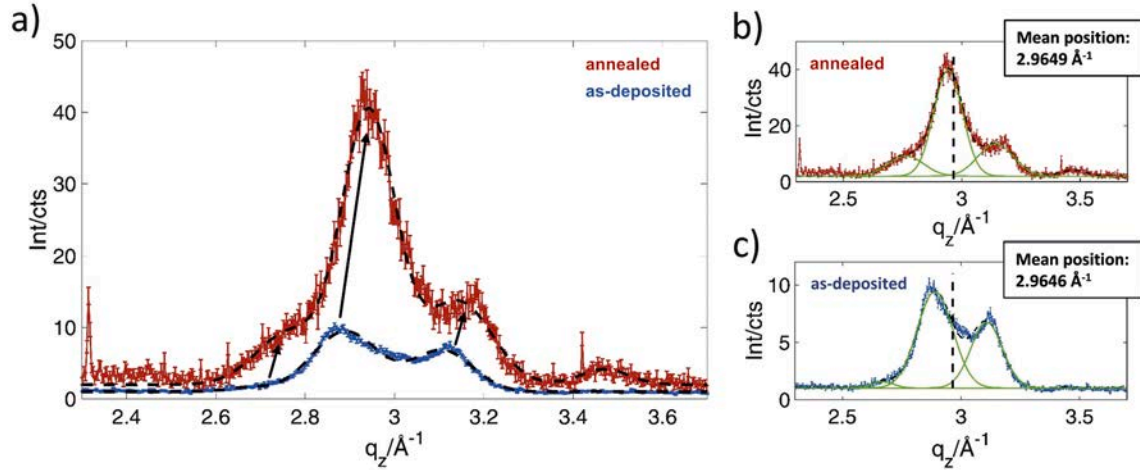
**Fig. 2.** (a) Diffracted intensity around the TiN (002) Bragg reflection. Laue oscillations are observed due to the periodic superlattice. The superlattice reflection intensity distribution is shown as a function of the scattering vector $q$. (blue) as-deposited and (red) heated multilayer. (b-c) Fit of the peak intensity modulation by the three Gaussian functions and linear background offset (green lines). The $q$-position of the TiN (002) reflection is indicated with the vertical dashed lines. (For interpretation of the references to colour in this figure legend, the reader is referred to the web version of this article.)

retaining the multilayer heterostructure (see Fig. 3g).

The shape and the spacing of the intensity modulation reflects the observed increase of $\Lambda$. A single FeCo Bragg reflection (or its Laue oscillation) could not be evidenced by XRD at its theoretical position observed for thick films or bulk samples. It is reasonable to suppose that the lack of intensity is due to poor long-range crystallinity of the FeCo component or due to changes of the CsCl-type crystal structure within the superlattice.

Low magnification scanning TEM images are shown in Fig. 3a and b

to provide a direct impression of the thin film morphology. The iterative sputter deposition of TiN and FeCo material directly onto the native Si/SiO$_2$ substrate is promoting a discrete multilayer film with columnar microstructure perpendicular to the substrate surface.

The diffuse intensities distributed on concentric rings of Fast Fourier Transform (FFT) pattern calculated from HRTEM micrographs evidence the absence polycrystalline texture within the first 10 bilayers of film growth as shown in Fig. 3c. In comparision, the FFTs from any region above these initial layers describe the evolution from randomly oriented
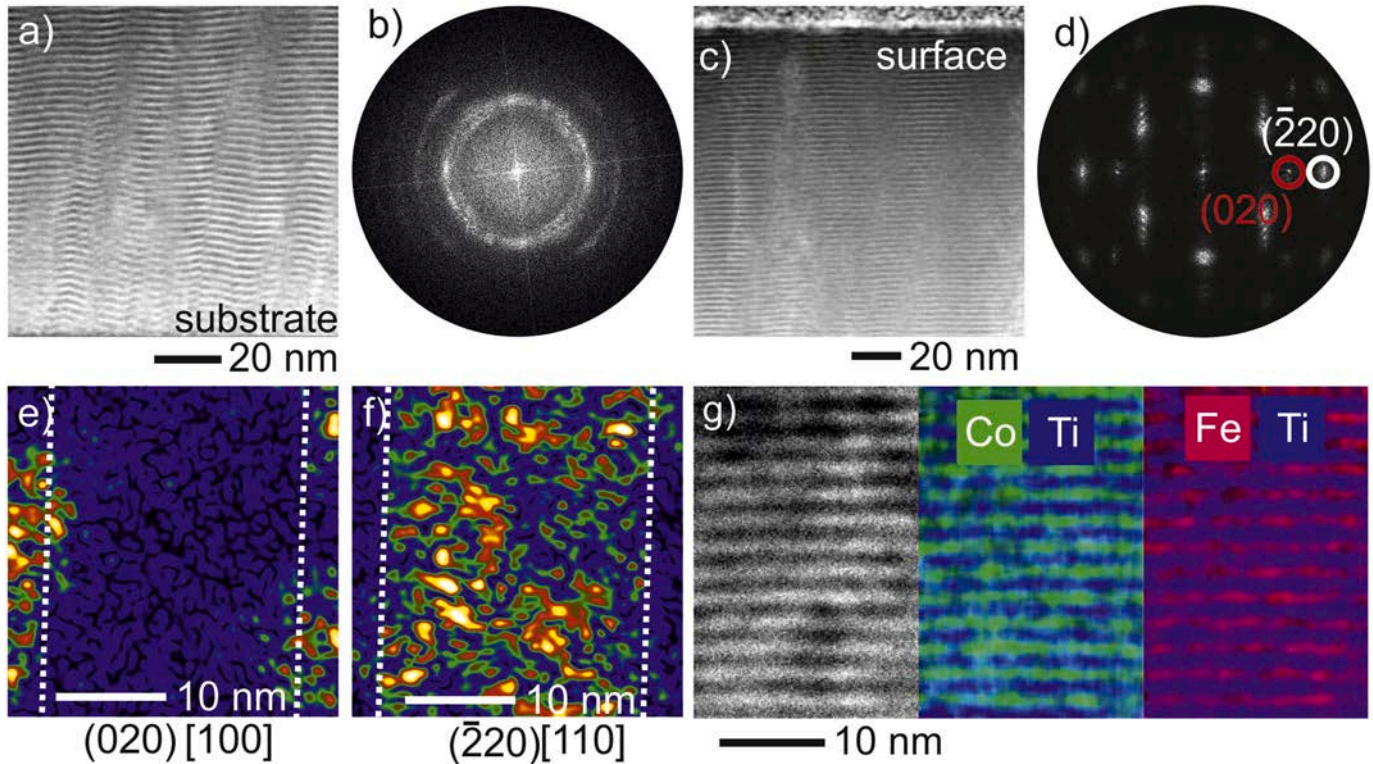


**Fig. 3.** Structure evolution of the FeCo/TiN multilayer . a,c) Overview STEM images recorded close to the substrate interface (a) and at top surface (c). b,d) FFT analysis of regions close to the substrate and film surface on the as-deposited multilayer. b) FFT obtained close to the substrate shows almost no specific texture. d) FFT obtained close to the film surface shows a strong $c$-texture. e,f) Intensity maps of the phase component of the respective (2 20) and (020) reflections visualize high intensity (bright regions) in columnar domains with [110] and [100] crystallographic orientation. The white dashed lines guide the eye to show the columnar domains g) EDS mapping showing the chemical distribution of Fe, Co and Ti in a multilayer architecture (annealed multilayer).

nanocrystalline grains into a highly *c*-textured crystalline structure (see Fig. 3d). The well-separated intensities in the FFT pattern display the formation of columnar grains (or regions) describing a *c*-axis texture, similar to thin films of AlN [8]. The individual columns favor defined azimuthal rotations around the *c*-direction described below and in Ref. [16]. The individual columns can be visualized by mapping out the origin of intensity of the in-plane (020) and ( 220) reflections, corresponding to columns with cubic TiN [100] and [110] orientations (Fig. 3e and f).

The morphology of the layers across *c* is characterized by distinct roughness. From the overview STEM images recorded at the bottom and top surface of the film, a higher roughness is observed within the first 30 nm of film growth and is flattening out with increasing film thickness. At the top side of the 400 nm thick film, quasi-parallel layers without noticeable roughness are established.

The elemental maps presented in Fig. 3g) show the distribution of Fe, Co and Ti for the heated multilayer. According to the EDS maps, the periodicity of FeCo and TiN layers is preserved after annealing showing no direct evidence of temperature effects such as interdiffusion or recrystallization accompanied with a breakdown of the layered structure.

### 3.2. Description of orientation relationships

SAED experiments yield information about the average local structure of the annealed multilayer composed of layers of TiN and FeCo. The SAED pattern is presented in Fig. 4a) and reflects the columnar microstructure showing the superposition of multiple zone axis (ZA) patterns specified by the [100], [110], [210] and [310] notations with respect to the principal component as already described in Ref. [16] and presented in Fig. A2. A columnar microstructure with small grain size is supported by the growth zone model by Thornton or Anders for small argon pressure and no substrate heating [23,24]. In extension of a simple superposition of individual ZA patterns the experimental SAED pattern features periodic intensity distributions along *c* (see Figs. 3d and 4a). This intensity modulation is indicative for a defined structural connection between the lattices of FeCo and TiN establishing a superlattice with a well defined periodicity length of $\Lambda \sim 2.26°nm$, which is in excellent

agreement with XRR experiments.

In addition, the tipped, elongated and diffuse shape of the reflections is rationalized by a small angle preceding rotational misalignment of the *c*-axis of the columnar grain structure [25,26] or by layer roughness. Overall, the SAED experiment demonstrated highly *c*-textured layers of FeCo and TiN consisting of at least three domains showing a dominant fibre texture [27]. The dominant *c*-axis fibre texture of the superlattice is further supported by pole-figure (PF) measurements of the as-deposited and annealed multilayer shown in Fig. A3.

The bilayer thickness $\Lambda$ and the different columnar domains of the as-deposited multilayer are imaged by aberration corrected high-resolution microscopy. Representative HRTEM micrographs are presented in Fig. 4b) and Fig. A4 showing the impact of aberration correction on the phase contrast micrographs, which allows a clear identification of individual layers. The HRTEM micrograph of Fig. 4b displays individual layers of TiN and FeCo with nearly monoatomic flat interfaces of the as-deposited multilayer. From the inset, two discernable oriented lattices with different out-of-plane lattice constants and a lattice orientation corresponding to the [100] and [110] orientations for the FeCo and TiN layers are identified, respectively. Further analysis of the periodic variations of the phase contrast in HRTEM micrographs presented in Fig. A5 hint that, at least locally, FeCo crystallizes in its low temperature ordered B2 phase forming a monoatomic interface with opposing Co and N atoms. These results suggest, that the in-plane lattice mismatch of 5.2% between these two structures is compensated by coherent in-plane lattice strains at the interface in one or both components which is resulting in a strained superlattice [28]. A cube-on-cube relationship is expected in a wide range of materials [29].

### 3.3. Structural modeling

The cube-on-cube relationship is described by a 45° rotational alignment between the experimentally observed TiN[100] and FeCo [110] oriented lattices and serves as starting point for structural modeling using the crystallographic relationships demonstrated in Fig. 5a and b. However, for an in-plane lattice misfit of 5.2% between the cubic structures large strains are expected at the interfaces. In some cases, the major amount of stress is compensated by only one component
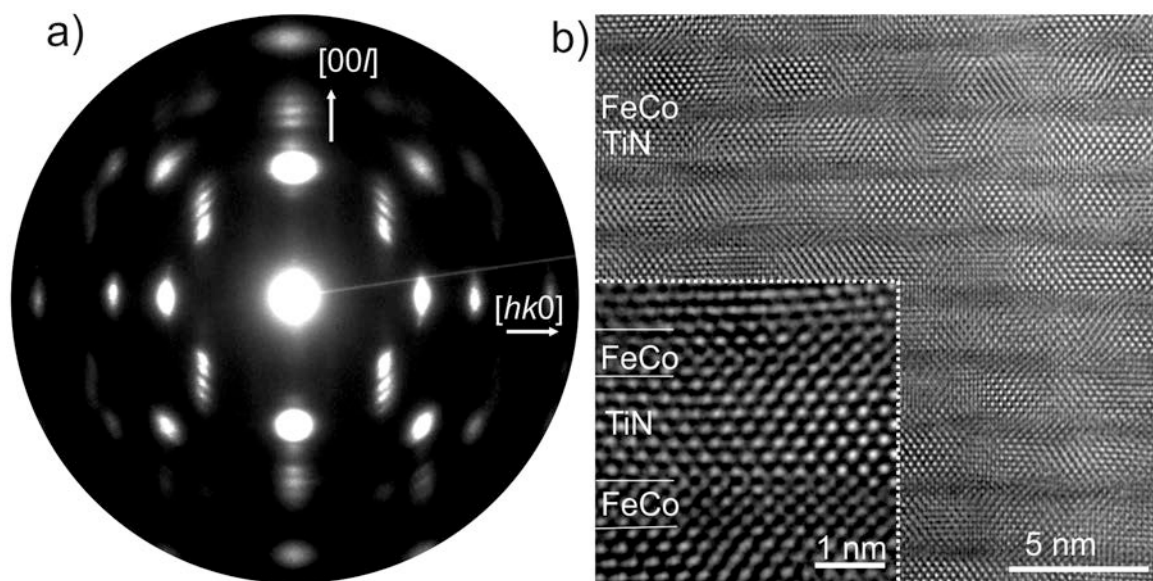


**Fig. 4.** a) SAED pattern recorded at the center of the as-deposited multilayer film. The SAED pattern is composed of the superposition of multiple zone axes [*uv*0]. The domains particularly display crystallographic orientations with respect to the TiN lattice of [100], [110] and [310] and show superlattice reflections along the [00*l*] direction arising from the nanoscale repetitive layering scheme with their corresponding FeCo counterpairs in [110], [100] and [210] orientation, respectively. b) HRTEM micrograph showing individual layers of FeCo and TiN. On average, the individual FeCo layers extend over two unit cells (~7 Å) and the TiN layers over three unit cells (~16 Å)..
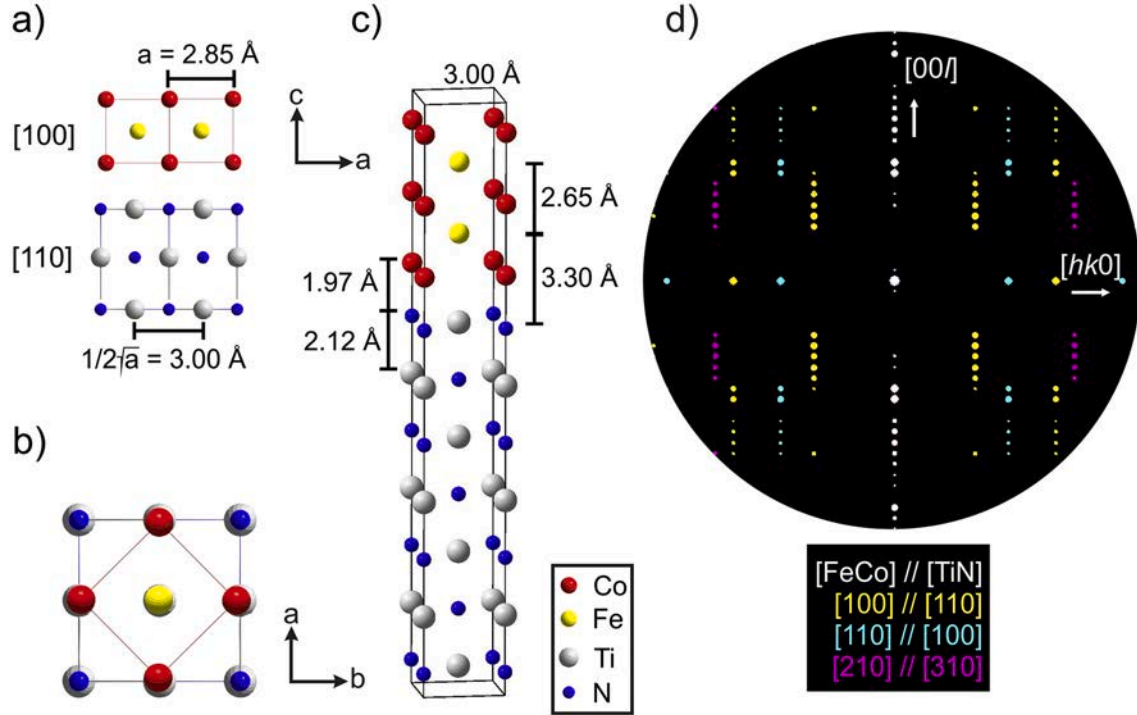
**Fig. 5.** a) Cubic unit cells of the FeCo and TiN lattice in [100] and [110] orientation. b) 45°-rotated cube-on-cube relationship in top-view showing a lattice mismatch of 3.00 Å // 2.85 Å. c) Supercell model based on pseudomorphic growth by in-plane lattice expansion of FeCo and compression of the *c*-parameter. d) Kinematic simulations of electron diffraction intensity for each zone axis based on the epitaxial relationship of the supercell model are superimposed in the presented pattern.

until a layer thickness of several angstroms is reached without formation of misfit dislocations. This phenomenon called *pseudomorphism*. [30] In this special case of epitaxy, the constrained in-plane lattice promotes the nanostabilization of metastable phases, e.g. tetragonal distorted variants [31–33]. From the experimental data, an in-plane lattice expansion from 2.85 Å to about 2.96 Å is determined for FeCo, which is matching with the TiN in-plane lattice constants. Based on these results, the pseudomorphic growth characteristic of the superlattice is introduced into a model describing the average structure of the as-despoited superlattice structure (Fig. 5c).

To relate the nanostructure data to the electron diffraction and X-ray scattering observations, a structural model for the as-deposited superlattice is designed and used for subsequent simulation. The design of this supercell model is described in the following steps: (1) A modification of the cubic [110]-oriented TiN unit cell is constructed to provide a common description of the components in [100] orientation. The new tetragonal TiN unit cell is described by lattice parameters of $a^t$ and $b^t$ 3.00 Å and by keeping $c_{TiN}$ 4.25 Å constant. (2) The [100]-oriented TiN unit cell is tripled in *c*-direction and connected to two unit cells of [100] FeCo at the (001) face. (3) In agreement with experimental evidence a coherently in-plane strained FeCo lattice is assumed, in approximation to a pseudomorphically grown heterostructure. Hence the $a^t$ and $b^t$ in-plane lattice constants are set to 3.00 Å. (4) In a simple physical consideration, the expansion of the in-plane lattice of the FeCo unit cell is accompanied by compressive strain on the out-of-plane parameter to preserve a constant volume. Indeed, atomic distances of 2.65 Å - 2.75 Å were measured in *c*-direction on the HRTEM data between.. Further spacings at the interface could be obtained as well and are implemented in the model using a compressed lattice parameter $c_{FeCo}$ 2.65 Å, which was the lowest observed lattice parameter to create a strongly tetragonal distorted FeCo variant. Overall, a structural model is set up by three tetragonal unit cell variants of the undistorted cubic TiN lattice connected to two tetragonal distorted unit cells of FeCo with total unit cell dimensions of $a_{SL}$ 3.00 Å, $b_{SL}$ 3.00 Å, $c_{SL}$ 22.00

Å. Implementing an unstrained $c_{FeCo}$ 2.85 Å into the supercell model results in minimal changes of the reflection positions and intensity due to the larger $c_{SL}$ 22.60 Å. Considering a constant unit cell volume and a resulting lattice parameter of 2.74 Å, it has to be assumed that the superlattice is not strained equally but is varying in between 2.85 Å and 2.65 Å giving rise to the diffuse superlattice reflections. The described incremental steps are assisted by knowledge obtained from kinematic simulation of electron diffraction pattern to check the models' validity. Note, one possibility to transfer this model to the annealed samples would require the introduction of further tensile lattice strains in the out-of-plane direction of the superlattice. However experimental evidence by direct imaging methods is missing for the specific multilayer sample.

The superposition of single kinematic simulations of zone axis patterns corresponding to the three major domains using the described supercell model is given in Fig. 5d) and shows acceptable agreement with the experimental pattern (Fig. 4a). The individual presentation of the rotated supercell model and the simulated ED patterns are shared in Fig. A6 for completeness. However, the supercell model is refined comparing highly localized measured HRTEM data with average SAED data and is regarded only as an approximation to the average structure. Further, the simulation is only exact to display the position of superlattice reflections but fails to quantify the experimental reflection intensity, because the simulation based on the supercell as single crystals and not as domains of strongly confined width.

### 3.4. Verification of compensated in-plane strain by geometric phase analysis

Besides the agreement between the position of periodic reflections arising in supercell based simulations and the experimental SAED pattern pointing to the formation of a superlattice with similar in-plane lattice constants, the variation of the in-plane lattice parameter *a* was calculated by geometric phase analysis (GPA) [34,35] mapping the in-

plane strain distribution in the superlattice with respect to the TiN lattice The GPA map was calculated using the (002) and ( 220) reflections of the FFT to display the variation of the in-plane component with respect to the strain tensor as depicted in Fig. 6. The mapped in-plane strain distribution shows alternating tensile and compressive strain along the thin FeCo layers on a scale of ±1% with respect to the reference TiN lattice (Fig. A7), which is a deviation of only about 0.03 Å. This finding reflects the in-plane lattice expansion of the tetragonal distorted FeCo unit cell determined by SAED, HRTEM and subsequent modeling under the premise of the pseudomorphic growth scheme. Further, indicators of in-plane strain are visualized in the TiN itself presumably indicating small angle tilts between individual grains.

The nanostabilization of body centered tetragonal (bct) variants of FeCo with $c/a > 1$ is intended to induce large perpendicular uniaxial magnetic anisotropies in ultra-thin nanoscale films leading to a huge magnetic hardening of FeCo films [31,36–39]. The required lattice deformation can be achieved by the right choice of underlayer, which should promote an in-plane compressive strain to the FeCo unit cell [40–42]. However, with increasing film thickness, the applied lattice strains quickly relax after some few nanometers (e.g. 3.4 nm) and the large perpendicular uniaxial magnetic anisotropy is lost [42,43]. Such film relaxation effects can be impeded by the incorporation with impurity atoms such as V, N or C to stabilize bct FeCo structures in films with a thickness of over 100 nm [44,45].

Contrary, there are also several approaches of strain engineering in order to soften the magnetic properties by thermal annealing, adequate underlayers or a multilayer architecture in combination with a non-magnetic or ferromagnetic material. In case of underlayers or multilayers, the magnetic softening can be reasoned by the simple decrease of grain size according to Hoffmann's ripple theory [4,46,47]. In this respect, multilayers of Co/FeCo starting on a layer of Co introduces smaller grain growth within the FeCo layer resulting in a very low in-plane coercivitiy along the hard axis in comparision to FeCo underlayer. [4] The same was observed for FeCo layers separated by Ag interlayers [6]. In a different approach, the in-plane magnetic anisotropy was reported to be reduced by the application of an external tensile strain in films of FePt. [48] In the former study on the magnetic properties on identical [FeCo/TiN]$_{384}$ films ($\Lambda$ 2.6 nm) deposited up to a film thickness of 1000 nm using the identical process, a coercive field of 0.30 mT with an in-plane anisotropy was reported. [1] The effect of layer thickness was also demonstrated in comparison to slightly thicker layers ($\Lambda$ 4.3 nm) of FeCo of showing a coercive field of 1.33 mT. It is expected, that the reduction of the coercive field is related to the smaller layer thickness. But the new insights on the atomic structure of FeCo in these nanolayers at least opens speculation about the contribution of the tetragonal distortion ($c/a < 1$) to the in-plane anisotropy. However, since atomic scale investigations on the FeCo structure are missing on these reported films, we can only speculate about the exact layer thickness and the critical layer thickness of FeCo on TiN, where relaxation of the tetragonal variant occurs. Also, there are no reports to our knowledge about the influence of an in-plane tetragonal lattice distortion with $c/a < 1$ on the magneto-crystalline anisotropy energy or its impact in comparison to the grain size. To differentiate between both contributions, the deposition of epitaxial lattice matched films, e.g. FeCo [100]/Mo[110] with identical layer thickness but cubic FeCo unit cells might be essential.

## 4. Conclusion

The microstructural evolution and the nanostructure growth epitaxy in sputter deposited FeCo/TiN ultra-thin films with bilayer periodicity of 2.26 Å have been investigated using the combination of aberration corrected TEM imaging, X-ray scattering and electron diffraction methods supported by modeling and structure simulations. These studies shed new light on the nanostructure of sputter-deposited growth of nanolayers of FeCo/TiN superlattices and result in the following observations:

- FeCo/TiN multilayers exhibit a columnar microstructure which is described by a strong fibre texture which is evolving after some nanometers.

- The FeCo/TiN nanolayers form a defined superlattice which was characterized by XRD and TEM. A 45°-rotated cube-on-cube orientation relationship between FeCo and TiN was verified, enabled by pseudomorphic growth resulting in tensile in-plane strain acting on the FeCo lattice to match with the TiN (001) plane. In this scheme, tetragonal distorted variants of FeCo are stabilized.
- Temperature induced lattice changes in FeCo/TiN multilayers have been observed and discussed by both electron diffraction and X-ray scattering methods.

**Data availability**

The raw/processed data required to reproduce these findings can be shared upon request to the corresponding authors.

**Prime novelty statement**

The prime novelty of this research is the identification of an established epitaxy relationship between nanolayers of FeCo and TiN by transmission electron microscopy. Both FeCo and TiN layers were found in their bulk crystal structure at layer thickness ~1 nm, but in-plane strain acting on the FeCo unit cell due to pseudomorphism stabilizes tetragonal distorted variants. The study was supported by structure modeling to explain complex electron diffraction pattern containing
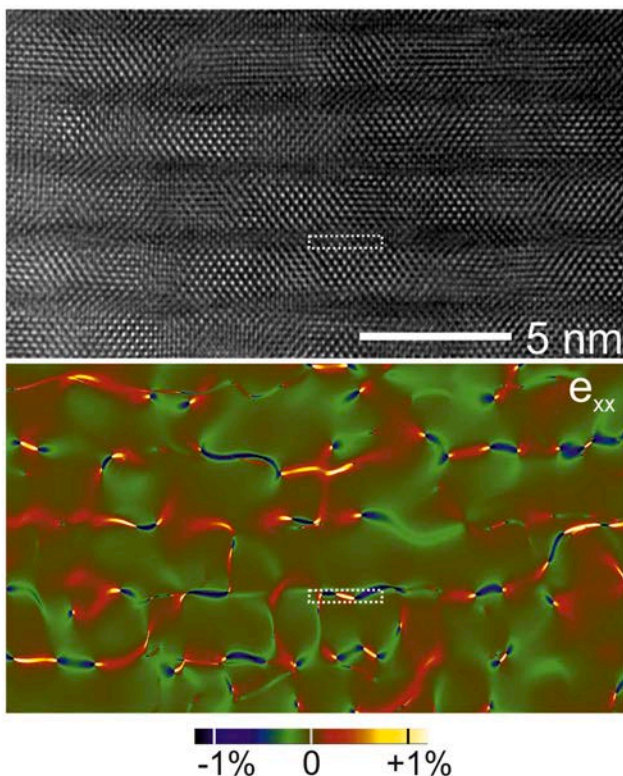


**Fig. 6.** HRTEM micrograph and corresponding map of in-plane lattice variations with respect to the TiN lattice demonstrated by geometric phase analysis. Almost negligible tensile and compressive strains alternate at the location of FeCo layers demonstrating pseudomorphism. Strain within the TiN layers is related to small mistilts within the cubic lattice. The dashed box marks the position of strain profiles depicted in Fig. A7.

superlattice reflections.

## Declaration of Competing Interest

The authors declare that they have no known competing financial interests or personal relationships that could have appeared to influence the work reported in this paper.

## Acknowledgments

## References

[1] C. Klever, M. Stüber, H. Leiste, E. Nold, K. Seemann, S. Ulrich, H. Brunken, A. Ludwig, C. Thede, E. Quandt, Multifunctional FeCo/TiN multilayer thin films with combined magnetic and protective properties, Adv. Eng. Mater. 11 (2009) 969–975, https://doi.org/10.1002/adem.200900214.

[2] V. Robisch, S. Salzer, N.O. Urs, J. Reermann, E. Yarar, A. Piorra, C. Kirchhof, E. Lage, M. Hoft, G.U. Schmidt, R. Knochel, J. McCord, E. Quandt, D. Meyners, Pushing the detection limit of thin film magnetoelectric heterostructures, J. Mater. Res. 32 (2017) 1009–1019, https://doi.org/10.1557/jmr.2017.58.

[3] J. Reermann, P. Durdaut, S. Salzer, T. Demming, A. Piorra, E. Quandt, N. Frey, M. Hoft, G. Schmidt, Evaluation of magnetoelectric sensor systems for cardiological applications, Measurement. 116 (2018) 230–238, https://doi.org/10.1016/j.measurement.2017.09.047.

[4] X. Liu, A. Morisako, Soft magnetic properties of FeCo films with high saturation magnetization, Journal of Applied Physics 103 (2008), 07E726, https://doi.org/10.1063/1.2839612.

[5] G. Pan, H. Du, (FeCo/Co–M)n soft magnetic multilayers with uniaxial anisotropy and very high saturation magnetization, Journal of Applied Physics 93 (2003) 5498–5502, https://doi.org/10.1063/1.1563824.

[6] M. Staruch, D.B. Gopman, Y.L. Iunin, R.D. Shull, S.F. Cheng, K. Bussmann, P. Finkel, Reversible strain control of magnetic anisotropy in magnetoelectric heterostructures at room temperature, Sci. Rep. 6 (2016) 1–9, https://doi.org/10.1038/srep37429.

[7] S. Marauska, T. Dankwort, H.J. Quenzer, B. Wagner, Sputtered thin film piezoelectric aluminium nitride as a functional MEMS material and CMOS compatible process integration, Procedia Engineering. 25 (2011) 1341–1344, https://doi.org/10.1016/j.proeng.2011.12.331.

[8] V. Hrkac, A. Kobler, S. Marauska, A. Petraru, U. Schürmann, V.S. Kiran Chakravadhanula, V. Duppel, H. Kohlstedt, B. Wagner, B.V. Lotsch, C. Kübel, L. Kienle, Structural study of growth, orientation and defects characteristics in the functional microelectromechanical system material aluminium nitride, J. Appl. Phys. 117 (2015) 014301, https://doi.org/10.1063/1.4905109.

[9] P. Hayes, V. Schell, S. Salzer, D. Burdin, E. Yarar, A. Piorra, R. Knochel, Y. K. Fetisov, E. Quandt, Electrically modulated magnetoelectric AlN/FeCoSiB film composites for DC magnetic field sensing, J. Phys. D. Appl. Phys. 51 (2018) 354002, https://doi.org/10.1088/1361-6463/aad456.

[10] B. Gojdka, R. Jahns, K. Meurisch, H. Greve, R. Adelung, E. Quandt, R. Knochel, F. Faupel, Fully integrable magnetic field sensor based on delta-E effect, Appl. Phys. Lett. 99 (2011) 223502, https://doi.org/10.1063/1.3664135.

[11] R. Jahns, S. Zabel, S. Marauska, B. Gojdka, B. Wagner, R. Knochel, R. Adelung, F. Faupel, Microelectromechanical magnetic field sensor based on ΔE effect, Appl. Phys. Lett. 105 (2014) 052414, https://doi.org/10.1063/1.4891540.

[12] S. Zabel, J. Reermann, S. Fichtner, C. Kirchhof, E. Quandt, B. Wagner, G. Schmidt, F. Faupel, Multimode delta-E effect magnetic field sensors with adapted electrodes, Appl. Phys. Lett. 108 (2016) 222401, https://doi.org/10.1063/1.4952735.

[13] B. Spetzler, C. Kirchhof, J. Reermann, P. Durdaut, M. Hoft, G. Schmidt, E. Quandt, F. Faupel, Influence of the quality factor on the signal to noise ratio of

magnetoelectric sensors based on the delta-E effect, Appl. Phys. Lett. 114 (2019) 183504, https://doi.org/10.1063/1.5096001.

[14] V. Hrkac, E. Lage, G. Koppel, J. Strobel, J. McCord, E. Quandt, D. Meyners, L. Kienle, Amorphous FeCoSiB for exchange bias coupled and decoupled magnetoelectric multilayer systems: real-structure and magnetic properties, J. Appl. Phys. 116 (2014) 134302, https://doi.org/10.1063/1.4896662.

[15] H. Fukuzawa, Y. Kamiguchi, K. Koi, H. Iwasaki, M. Sahashi, Saturation magnetostriction of an ultrathin CoFe free-layer on double-layered underlayers, J. Appl. Phys. 91 (2002) 3120–3124, https://doi.org/10.1063/1.1434551.

[16] C. Klever, K. Seemann, M. Stüber, S. Ulrich, H. Brunken, A. Ludwig, H. Leiste, Epitaxially stabilized TiN/(Ti,Fe,Co)N multilayer thin films in (pseudo-)fcc crystal structure by sequential magnetron sputter deposition, J. Phys. D. Appl. Phys. 43 (2010) 395406, https://doi.org/10.1088/0022-3727/43/39/395406.

[17] C.L. Jia, L. Houben, A. Thust, J. Barthel, On the benefit of the negative-spherical-aberration imaging technique for quantitative HRTEM, Ultramicroscopy. 110 (2010) 500–505, https://doi.org/10.1016/j.ultramic.2009.10.006.

[18] M. Garbrecht, E. Spiecker, K. Tillmann, W. Jager, Quantitative atom column position analysis at the incommensurate interfaces of a (PbS)1.14NbS2 misfit layered compound with aberration-corrected HRTEM, Ultramicroscopy 111 (2011) 245–250, https://doi.org/10.1016/j.ultramic.2010.11.031.

[19] P.A. Stadelmann, EMS - a software package for electron diffraction analysis and HREM image simulation in materials science, Ultramicroscopy. 21 (1987) 131–145, https://doi.org/10.1016/0304-3991(87)90080-5.

[20] R. Kilaas, Optimal and near-optimal filters in high-resolution electron microscopy, J. Microsc. 190 (1998) 45–51, https://doi.org/10.1046/j.1365-2818.1998.3070861.x.

[21] L.G. Parratt, Surface studies of solids by Total reflection of X-rays, Phys. Rev. 95 (1954) 359–369, https://doi.org/10.1103/PhysRev.95.359.

[22] I.K. Schuller, New class of layered materials, Phys. Rev. Lett. 44 (1980) 1597–1600, https://doi.org/10.1103/PhysRevLett.44.1597.

[23] J.A. Thornton, High rate thick film growth, Annu. Rev. Mater. Sci. 7 (1977) 239–260, https://doi.org/10.1146/annurev.ms.07.080177.001323.

[24] A. Anders, A structure zone diagram including plasma-based deposition and ion etching, Thin Solid Films 518 (2010) 4087–4090, https://doi.org/10.1016/j.tsf.2009.10.145.

[25] S. Stavroyiannis, C. Christides, D. Niarchos, Th. Kehagias, Ph. Komninou, Th. Karakostas, Low-field giant magnetoresistance in (111)-textured Co/Au multilayers prepared with magnetron sputtering, J. Appl. Phys. 84 (1998) 6221–6228, https://doi.org/10.1063/1.368940.

[26] E. Yarar, V. Hrkac, C. Zamponi, A. Piorra, L. Kienle, E. Quandt, Low temperature aluminum nitride thin films for sensory applications, AIP Adv. 6 (2016), 075115, https://doi.org/10.1063/1.4959895.

[27] C. Detavernier, A.S. Ozcan, J. Jordan-Sweet, E.A. Stach, J. Tersoff, F.M. Ross, C. Lavoie, An off-normal fibre-like texture in thin films on single-crystal substrates, Nature. 426 (2003) 641–645, https://doi.org/10.1038/nature02198.

[28] J.M. Vandenberg, D. Gershoni, R.A. Hamm, M.B. Panish, H. Temkin, Structural perfection of InGaAs/InP strained-layer superlattices grown by gas source molecular-beam epitaxy: a high-resolution x-ray diffraction study, J. Appl. Phys. 66 (1989) 3635–3638, https://doi.org/10.1063/1.344072.

[29] C.J. Palmstrom, Epitaxy of dissimilar materials, Annu. Rev. Mater. Sci. 25 (1995) 389–415, https://doi.org/10.1146/annurev.ms.25.080195.002133.

[30] K.L. Chopra, Metastable thin film epitaxial structures, Phys. Stat. Sol. (b). 32 (1969) 489–507, https://doi.org/10.1002/pssb.19690320202.

[31] G. Andersson, T. Burkert, P. Warnicke, M. Bjorck, B. Sanyal, C. Chacon, C. Zlotea, L. Nordstrom, P. Nordblad, O. Eriksson, Perpendicular magnetocrystalline anisotropy in tetragonally distorted Fe-Co alloys, Physical Review Letters 96 (2006), https://doi.org/10.1103/PhysRevLett.96.037205.

[32] G. Andersson, M. Bjorck, H. Lidbaum, B. Sanyal, C. Chacon, C. Zlotea, S. Valizadeh, Structure of Fe–Co/Pt(001) superlattices: a realization of tetragonal Fe–Co alloys, J. Phys.: Condens. Matter. 19 (2007), 016008, https://doi.org/10.1088/0953-8984/19/1/016008.

[33] E.G. Fu, N. Li, A. Misra, R.G. Hoagland, H. Wang, X. Zhang, Mechanical properties of sputtered Cu/V and Al/Nb multilayer films, Mater. Sci. Eng. A 493 (2008) 283–287, https://doi.org/10.1016/j.msea.2007.07.101.

[34] M.J. Hÿch, I. Potez, Geometric phase analysis of high-resolution electron microscopy images of antiphase domains: example Cu3Au, Philosophical Magazine A. 76 (1997) 1119–1138, https://doi.org/10.1080/01418619708214218.

[35] M.J. Hÿch, E. Snoeck, R. Kilaas, Quantitative measurement of displacement and strain fields from HREM micrographs, Ultramicroscopy. 74 (1998) 131–146, https://doi.org/10.1016/S0304-3991(98)00035-7.

[36] M. Matsuura, N. Tezuka, S. Sugimoto, Increased uniaxial perpendicular anisotropy in tetragonally distorted FeCo-Ti-N films, Journal of Applied Physics 117 (2015), 17A738, https://doi.org/10.1063/1.4916763.

[37] G. Andersson, M. Bjorck, Anisotropy Tuning in Tetragonal FeCo Alloys, 2010, https://doi.org/10.1166/jnn.2010.2587.

[38] T. Burkert, L. Nordstrom, O. Eriksson, O. Heinonen, Giant magnetic anisotropy in tetragonal FeCo alloys, Phys. Rev. Lett. 93 (2004), 027203, https://doi.org/10.1103/PhysRevLett.93.027203.

[39] E. Şaşıoğlu, C. Friedrich, S. Blügel, Strong magnon softening in tetragonal FeCo compounds, Phys. Rev. B 87 (2013), 020410, https://doi.org/10.1103/PhysRevB.87.020410.

[40] X. Liu, H. Kanda, A. Morisako, The effect of underlayers on FeCo thin films, J. Phys.: Conf. Ser. 266 (2011), 012037, https://doi.org/10.1088/1742-6596/266/1/012037.

[41] P. Warnicke, G. Andersson, M. Bjorck, J. Ferré, P. Nordblad, Magnetic anisotropy of tetragonal FeCo/Pt(001) superlattices, J. Phys.: Condens. Matter. 19 (2007), 226218, https://doi.org/10.1088/0953-8984/19/22/226218.

[42] A. Winkelmann, M. Przybylski, F. Luo, Y. Shi, J. Barthel, Perpendicular magnetic anisotropy induced by tetragonal distortion of FeCo alloy films grown on Pd(001), Phys. Rev. Lett. 96 (2006) 257205, https://doi.org/10.1103/PhysRevLett.96.257205.

[43] B. Lao, J.W. Jung, M. Sahashi, Strong Perpendicular Uniaxial Magnetic Anisotropy in Tetragonal Fe0.5Co0.5 Films of Artificially Ordered B2 State, IEEE Transactions on Magnetics 50 (2014) 1–4, https://doi.org/10.1109/TMAG.2014.2322936.

[44] T. Hasegawa, T. Niibori, Y. Takemasa, M. Oikawa, Stabilisation of tetragonal FeCo structure with high magnetic anisotropy by the addition of V and N elements, Sci. Rep. 9 (2019) 1–9, https://doi.org/10.1038/s41598-019-41825-7.

[45] L. Reichel, G. Giannopoulos, S. Kauffmann-Weiss, M. Hoffmann, D. Pohl, A. Edstrom, S. Oswald, D. Niarchos, J. Rusz, L. Schultz, S. Fahler, Increased magnetocrystalline anisotropy in epitaxial Fe-co-C thin films with spontaneous strain, J. Appl. Phys. 116 (2014) 213901, https://doi.org/10.1063/1.4901595.

[46] H.S. Jung, W.D. Doyle, J.E. Wittig, J.F. Al-Sharab, J. Bentley, Soft anisotropic high magnetization cu/FeCo films, Appl. Phys. Lett. 81 (2002) 2415–2417, https://doi.org/10.1063/1.1510163.

[47] H.S. Jung, W.D. Doyle, S. Matsunuma, Influence of underlayers on the soft properties of high magnetization FeCo films, J. Appl. Phys. 93 (2003) 6462–6464, https://doi.org/10.1063/1.1557653.

[48] P.V. Lukashev, N. Horrell, R.F. Sabirianov, Tailoring magnetocrystalline anisotropy of FePt by external strain, Journal of Applied Physics 111 (2012), 07A318, https://doi.org/10.1063/1.3673853.